

# Competing nodal d-wave superconductivity and antiferromagnetism: a Quantum Monte Carlo study

Xiao Yan Xu and Tarun Grover

*Department of Physics, University of California at San Diego, La Jolla, California 92093, USA*

(Dated: September 16, 2020)

Unconventional superconductors such as cuprates often host competing nodal superconductivity and antiferromagnetism. These systems are typically modeled as a repulsive Hubbard model whose unbiased simulation suffers from the fermion sign-problem at any non-zero doping. Here we will exploit the fact that neither of these phases, the nodal d-wave superconductor or the antiferromagnet, require any doping for their existence, and construct a sign-problem-free repulsive Hubbard model with an additional bosonic field which hosts both of these phases. Using Quantum Monte Carlo (QMC) simulations, supplemented with mean-field theory and continuum field-theory arguments, we find that it hosts three distinct phases: a nodal d-wave phase, an antiferromagnet, and an intervening phase which hosts coexisting antiferromagnetism and nodeless d-wave superconductivity. The transition from the coexisting phase to the antiferromagnet is described by the 2+1-D XY universality class, while the one from the coexisting phase to the nodal d-wave phase is described by the chiral Gross-Neveu-Heisenberg theory.

*Introduction*— The interplay between unconventional superconductivity and magnetism plays a crucial role in a wide variety of strongly correlated systems [1] such as cuprates [2, 3], heavy fermion materials [4–16], layered organic conductors [17–25], iron-based superconductors [26–30], Helium-3 [31] and even in recently studied twisted 2D materials [32]. Superconductors with nodal quasiparticles are particularly interesting since the fermionic quasiparticles cannot be neglected even for the ground state properties of the superconductor, or for understanding quantum phase transitions to proximate phases. In this paper, we will introduce a model which does not suffer from the fermion sign problem, and which demonstrably hosts both a nodal d-wave superconductor, and an antiferromagnetic insulator on a 2d square lattice, with an intermediate phase with coexisting antiferromagnetic and a gapped d-wave superconducting order parameter. We will study the phase diagram of the model using Quantum Monte Carlo (QMC) simulations.

One route to obtain an unconventional superconductor is to dope a Mott insulator [3, 33], as is experimentally the case for cuprates where nodal d-wave superconductor (dSC) arises upon doping. From a numerical perspective, this is rather challenging to pursue: the combination of ‘Mottness’ and continuously varying filling leads to the fermion sign problem. In fact, to date, there does not exist any model which has repulsive onsite electron-electron interactions at a generic filling which does not suffer from the fermion sign problem. However, one notes that two of the most prominent symmetry breaking phases in cuprates, namely the dSC or the AFM insulator in principle do *not* require doping for their existence: in the dSC, the charge  $U(1)$  symmetry is spontaneously broken, and therefore, there is no Luttinger theorem, while an AFM insulator in fact requires one to be at a commensurate filling (such as zero doping). Furthermore, the dSC and the AFM are ‘sign problem compatible’: both of these orders

are facilitated by an onsite repulsion. Finally, on a square lattice at half-filling, the ordering wavevector  $Q = (\pi, \pi)$  for the AFM matches the momentum difference between the nodes of the dSC, and therefore the onset of AFM will gap out the nodes in dSC. These observations suggest that one should be able to find a model without sign-problem which hosts these two competing phases. From an experimental perspective, competing dSC and AFM phases at half-filling are relevant to Mott insulators such as layered organic conductors  $\kappa$ -ET<sub>2</sub>Cu[N(CN)<sub>2</sub>]Cl and its derivatives [17–25] that undergo insulator to superconductor transition under an applied pressure.

Our model is partially motivated by the ideas presented in Ref.[34] where the phase diagram of competing dSC and AFM at a half-filling was studied using field-theoretic arguments. Through state-of-the-art Determinantal Quantum Monte Carlo (DQMC) simulations, we find three different phases in our model only by tuning a single parameter. In between the nodal dSC and the AFM, we find an intermediate phase with the coexistence of gapped dSC and AFM (dSC<sub>g</sub>+AFM). The phase transition between dSC<sub>g</sub>+AFM and AFM appears to be continuous and in the 3D XY universality class. The phase transition between nodal dSC and dSC<sub>g</sub>+AFM also appears to be continuous, while having more interesting critical behavior.

*Model*— Our model is defined on a square lattice and consists of four parts,  $H = H_t + H_V + H_U + H_{XY}$ . Here  $H_t + H_U = -t \sum_{\langle ij \rangle, \sigma} (c_{i, \sigma}^\dagger c_{j, \sigma} + \text{h.c.}) + \frac{U}{2} \sum_i (\rho_{i, \uparrow} + \rho_{i, \downarrow} - 1)^2$  is the standard Hubbard model with nearest neighbor hopping, with  $\rho_{i, \sigma} = c_{i, \sigma}^\dagger c_{i, \sigma}$ .  $H_V$  is the coupling between d-wave pairing and rotor type bosonic fields  $\theta$  living on the bonds of the square lattice,  $H_V = V \sum_{\langle ij \rangle} (\tau_{i, j} e^{i\theta_{ij}} (c_{i, \uparrow}^\dagger c_{j, \downarrow}^\dagger - c_{i, \downarrow}^\dagger c_{j, \uparrow}^\dagger) + \text{h.c.})$  with  $\tau_{i, i \pm \hat{x}} = 1$ ,  $\tau_{i, i \pm \hat{y}} = -1$ .  $H_{XY}$  is a quantum rotor Hamiltonian, describing the dynamics and interactions of fields  $\theta$ :  $H_{XY} = K \sum_{\langle ij \rangle} n_{ij}^2 - J \sum_{\langle ij, kl \rangle} \cos(\theta_{ij} - \theta_{kl})$ , where

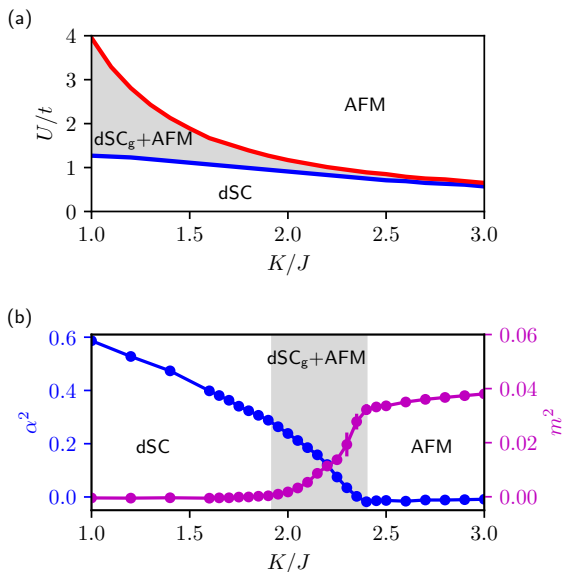


FIG. 1. Phase diagram of our model. (a) Mean-field phase diagram. dSC stands for the nodal  $d_{x^2-y^2}$  superconductor, AFM for the antiferromagnetic insulator, and dSC<sub>g</sub>+AFM for the coexisting gapped d-wave superconductor and antiferromagnetic insulator. (b) Quantum Monte Carlo phase diagram for  $U/t = 4.0$ .  $\alpha$  is the dSC order parameter,  $m$  is the AFM order parameter.

$[n_{ij}, e^{\pm i\theta_{ij}}] = \pm e^{\pm i\theta_{ij}}$ . The model has the conventional spin-rotation SU(2) symmetry and a charge U(1) symmetry given by  $c_{i,\sigma} \rightarrow c_{i,\sigma} e^{i\varphi}$ ,  $\theta \rightarrow \theta + 2\varphi$ . It also has a particle-hole symmetry  $c_{i,\sigma} \rightarrow \epsilon_i c_{i,\sigma}^\dagger$ ,  $\theta \rightarrow -\theta$ , at half-filling, where  $\epsilon_i = (-)^i$ . Perhaps most importantly, the model also hosts an anti-unitary symmetry  $\mathcal{U} : c_{i,\uparrow} \rightarrow \epsilon_i c_{i,\downarrow}^\dagger$ ,  $c_{i,\downarrow} \rightarrow -\epsilon_i c_{i,\uparrow}^\dagger$ ,  $i \rightarrow -i$  and  $\mathcal{U}^2 = -1$ , which makes the model sign problem-free [35], so that it can be simulated with large-scale DQMC methods.

One may obtain some features of the global phase diagram of our model without detailed calculations. Setting  $U = 0$ , when  $K/J \ll 1$ , the charge-U(1) symmetry will be spontaneously broken, and therefore, the fermion-part of the Hamiltonian reduces to the BCS mean-field theory for a nodal  $d_{x^2-y^2}$  superconductor, which we denote as dSC. The dSC phase is expected to be stable at small  $U$  since weak interactions are irrelevant for the nodal Dirac fermions. When  $K/J$  increases, eventually the charge-U(1) symmetry is expected to get restored due to fluctuations of the  $\theta$  field. Since the unit-cell of  $H$  contains an odd number of fermions, a gapped trivial paramagnet is ruled out [36, 37], and energetically, we expect that the phase at  $U/t \gg 1$  and  $K/J \gg 1$  to be a conventional antiferromagnet. Furthermore, since the nodes in dSC are separated by  $(\pi, \pi)$ , which is the ordering wavevector for AFM, one may also expect a phase where AFM coexists with a *gapped* d-wave superconductor. As well

we see, these expectations are born out by the DQMC calculations, but first, we consider a mean-field theory.

*Mean-field phase diagram*— Defining  $\hat{\alpha}_{ij} \equiv -e^{i\theta_{ij}}$  and  $\hat{\Delta}_{ij} \equiv \tau_{i,j}(c_{i,\uparrow}^\dagger c_{j,\downarrow}^\dagger - c_{i,\downarrow}^\dagger c_{j,\uparrow}^\dagger)$ , we are led to two coupled mean-field Hamiltonians, one for the fermions,  $H_f^{\text{MF}}$  and the other for the rotors,  $H_\theta^{\text{MF}}$ :

$$H_f^{\text{MF}} = -t \sum_{\langle ij \rangle, \sigma} (c_{i,\sigma}^\dagger c_{j,\sigma} + \text{h.c.}) - Um \sum_i (-)^i (\rho_{i,\uparrow} - \rho_{i,\downarrow}) - V\alpha \sum_{\langle ij \rangle} (\hat{\Delta}_{ij} + \text{h.c.}), \quad (1)$$

$$H_\theta^{\text{MF}} = K \sum_{\langle ij \rangle} n_{ij}^2 - J \sum_{\langle ij,kl \rangle} \cos(\theta_{ij} - \theta_{kl}) - V\Delta \sum_{\langle ij \rangle} (\hat{\alpha}_{ij} + \text{h.c.}), \quad (2)$$

where  $\alpha = \langle \hat{\alpha}_{ij} \rangle$ ,  $\Delta = \langle \hat{\Delta}_{ij} \rangle$  and  $m = \langle (-)^i (\rho_{i,\uparrow} - \rho_{i,\downarrow}) \rangle$ , and we have chosen the antiferromagnetic order parameter to point along the  $z$ -axis in the spin-space. We can solve the two coupled mean-field Hamiltonian self-consistently. The  $H_\theta^{\text{MF}}$  part is still an interacting rotor lattice problem which we solve using numerical exact diagonalization (ED) on a small cluster consisting of four bonds of a square lattice. After we obtain the value of  $\alpha$ , we solve the fermion part  $H_f^{\text{MF}}$ , and find a self-consistent solution. We set  $t = 1$ ,  $J = 1$ ,  $V/t = 0.5$ , and explore the  $U/t - K/J$  phase diagram as shown in Fig. 1(a). At small  $U/t$ , the (nodal) dSC is a stable phase, while at larger  $U/t$ , we enter a phase with coexisting gapped d-wave superconductivity (dSC<sub>g</sub>) and antiferromagnetism (AFM). At still larger  $U/t$ , a pure AFM phase without any superconductivity is stabilized. Tuning  $K/J$  changes the relative sizes of these three phases. Overall, when we increase  $K/J$ , the pure AFM region becomes larger, while the coexistence phase region (dSC<sub>g</sub>+AFM) shrinks. We note that a variational cluster perturbation theory and cluster dynamical mean-field theory calculations on doped repulsive Hubbard model also find a coexistence phase similar to ours (dSC<sub>g</sub>+AFM) [38–43].

*Quantum Monte Carlo phase diagram*— The model can be simulated with the DQMC method without sign problem (See Refs. [44–46] for additional technical details of DQMC). In DQMC, the imaginary time evolution is Trotter decomposed into  $L_\tau$  slices,  $\beta t = L_\tau \Delta_\tau$ , where imaginary time step  $\Delta_\tau = 0.1$  is used in our simulations. For the repulsive Hubbard term, we employ a SU(2) symmetric Hubbard-Stratonovich (HS) transformation to decouple it into fermion bilinears coupled to auxiliary fields. To explore the ground state properties, we scale the inverse temperature with the linear system size  $L$ , in particular, we fix  $\beta t = 2L$  and perform simulations up to  $L = 20$ . Motivated by the mean-field phase diagram in the  $U/t$ - $K/J$  plane, one only needs to tune

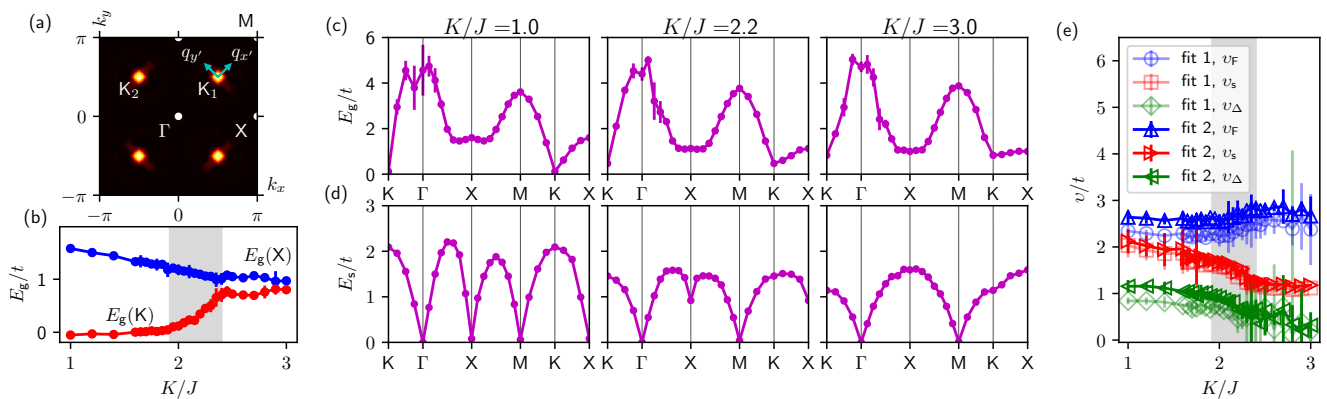


FIG. 2. Single-particle and spin gaps and velocities. (a) The first Brillouin zone (BZ) of the square lattice. Four light points are the location of nodes, and the lightness of the color denotes integrated spectral weight  $A(\vec{k}, \omega)$  over a small energy window near the Fermi level  $(0, 0.5t)$ . (b) Single-particle gap at the nodal point (K) and the anti-nodal point (X) extrapolated to thermodynamic limit. (c) Single-particle gap along the path K- $\Gamma$ -X-M-K-X of BZ at  $L = 16$ . (d) Spin gap along the same path of BZ at  $L = 16$ . (e) Fermi velocity, spin-wave velocity and pairing velocity extracted using two different fitting schemes.

one parameter to explore all three possible phases. We fix parameters  $U/t = 4.0$ ,  $V/t = 0.5$ , and explore possible phases by tuning only  $K/J$ . We define the AFM order parameter as  $\vec{m} = \langle (-)^i \vec{S}_i \rangle$ , and dSC order parameter as  $\alpha = \langle \hat{\alpha}_{ij} \rangle$ . In the simulation we can extract these order parameters from static correlation functions

$$m^2 = \frac{1}{L^4} \sum_{i,j} (-)^{i+j} \langle \vec{S}_i \cdot \vec{S}_j \rangle, \quad (3)$$

$$\alpha^2 = \frac{1}{4L^4} \sum_{\langle ij \rangle, \langle kl \rangle} \langle e^{i\theta_{ij}} e^{i\theta_{kl}} \rangle \quad (4)$$

Fig. 1(b) shows these order parameters extrapolated to the thermodynamic limit, see [44] for technical details. For  $K/J < 1.92(5)$ , only  $\alpha \neq 0$ , which corresponds to the nodal dSC phase. This is also evident from the spectral function integrated over a small energy window, Fig.2(a), which shows four distinct nodes. For  $1.92(5) < K/J < 2.40(5)$ , we have both  $\alpha \neq 0$  and  $m \neq 0$ , and therefore this is the dSC<sub>g</sub>+AFM phase. For  $K/J > 2.40(5)$ , we enter the pure AFM phase where only  $m \neq 0$ .

The phase diagram is also consistent with the results for the single-particle gap as well as the spin-gap, see Figs. 2(b), (c), (d). As shown in Fig. 2(c), in the nodal dSC region  $K/J < 1.92(5)$ , we have nodes at the K points, while the antinodal points X are gapped. The single particle gaps open both in the dSC<sub>g</sub>+AFM and the AFM regions. Similarly, the gap to spinful-excitations remains zero at  $\Gamma$  and M points in the dSC<sub>g</sub>+AFM and the AFM regions, due to the Goldstone modes resulting from the spin-rotation symmetry breaking.

*Phase transitions*— The transitions from the dSC to the dSC<sub>g</sub>+AFM and from the dSC<sub>g</sub>+AFM to the AFM

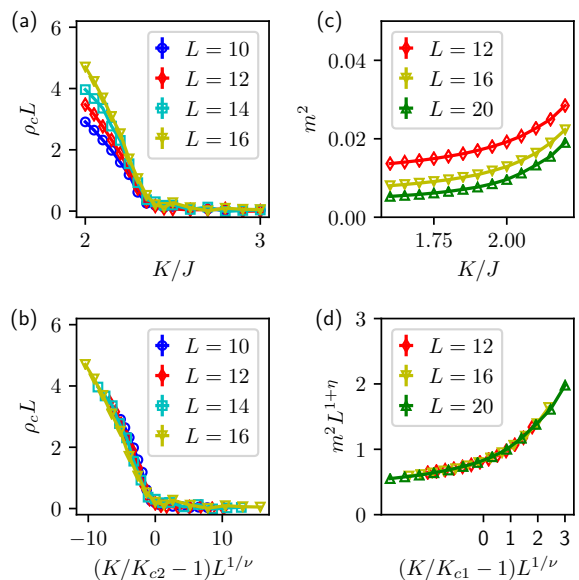


FIG. 3. Data collapse to obtain critical exponents. (a) Charge stiffness  $\rho_c$  for different system sizes near the second phase transition from the coexistence phase to the AFM phase. (b) Data collapse of the charge stiffness in (a) with  $K_{c2} = 2.40(5)$  leads to  $\nu \approx 0.67$ . (c) Squared AFM order parameter  $m^2$  near the transition from the nodal dSC phase to the coexistence phase. (d) Data collapse of  $m^2$  in (c) with  $K_{c1} = 1.92(5)$  leads to  $\nu = 0.99(8)$  and  $\eta = 0.55(2)$ .

both appear to be continuous. The transition from the dSC<sub>g</sub>+AFM to the AFM is the conventional XY transition, and the data for the charge stiffness can be collapsed quite well with 3D XY exponents, as shown in Fig. 3(a) and (b). The transition from the dSC to the dSC<sub>g</sub>+AFM is a more interesting one, which on theoretical ground we

believe to be in the chiral Gross-Neveu-Heisenberg universality class (see below). Using data collapse, we extract the critical exponents for this transition, as shown in Figs. 3(c) and (d). We estimate the correlation length exponent  $\nu = 0.99(8)$  and the anomalous dimension of the AFM order-parameter  $\eta_m = 0.55(2)$ .

We also measured the Fermi velocity  $v_F$ , the dSC pairing velocity  $v_\Delta$  defined via the nodal dispersion  $E_g(\vec{q}') = \sqrt{v_F^2 q_x'^2 + v_\Delta^2 q_y'^2 + E_g^2(\text{K})}$ , and the spin-wave velocity  $v_s$  defined via the dispersion of Goldstone modes at the M point through  $E_s(\vec{q}') = \sqrt{v_s^2 q'^2 + E_s^2(\text{M})}$ . To extract these velocities, we considered two different finite size scaling schemes. In scheme 1, we fix  $\delta q = \frac{2\pi}{L_{\text{max}}}$ , and for system sizes less than  $L_{\text{max}} = 20$ ,  $E_g(\text{K} + \vec{d}\vec{k}_2)$ ,  $E_g(\text{K} + \vec{d}\vec{k}_2)$  and  $E_s(\Gamma + \vec{d}\vec{k}_1)$  are obtained by interpolation. After we obtain gap functions for each system size, we perform an  $1/L$  extrapolation of the gap, and finally use the above formulas to obtain the velocities. In scheme 2, we first calculate the velocities based on the above formulas, and then perform the  $1/L$  extrapolation of the velocities. The velocities obtained from these schemes are shown in Fig. 2(e). Although our data suffers from finite-size effects due to the curvature of the dispersion [44], we see a tendency for the velocity differences to decrease on approaching the transition from dSC to dSC<sub>g</sub>+AFM. This is in line with the field theory prediction that at long distances, all three velocities become equal at this transition [34].

*Low energy theory*— The transition from the nodal dSC to the dSC<sub>g</sub>+AFM is of particular interest since it hosts gapless nodal fermions. The corresponding low energy theory is already discussed in Ref. [34]. In the following we will show that it can be mapped to the chiral Gross-Neveu-Heisenberg theory. The nodal dSC phase has nodes located at  $(\pm\frac{\pi}{2}, \pm\frac{\pi}{2})$ , as shown in Fig. 2. These four nodes are divided into two pairs, and form two four-component Dirac fermions. At the transition from the nodal dSC to the dSC<sub>g</sub>+AFM, in addition to the gapless nodal Dirac fermions, we also have gapless AFM modes  $\vec{N}$ , which couple linearly to the Dirac fermion bilinear possessing the same symmetry. After several steps of basis transformations [34], while ignoring the difference between the three velocities  $v_F, v_\Delta, v_s$ , and rescaling them to unity, one arrives at the following Lagrangian:

$$\mathcal{L} = \bar{\Psi} \not{\partial} \Psi + \frac{1}{2} (\partial_\mu \vec{N})^2 + u (\vec{N}^2)^2 + g \vec{N} \cdot (\Psi^\dagger \tau^y \vec{\sigma} \Psi) + \text{h.c.}, \quad (5)$$

where  $\not{\partial} = \gamma^\mu \partial_\mu$ , and the Pauli matrices  $\vec{\sigma}$  act in the particle-hole space of the original microscopic fermions  $c$ . The  $4 - \epsilon$  RG calculations predict that the difference between velocities eventually flows to zero, so that the above isotropic description is valid for a continuous transition. The isotropic free Dirac fermions in fact have an  $O(8)$  symmetry, which can be made man-

ifest by employing Majorana basis ( $\Psi = \eta_1 + i\eta_2$ ). We will now exploit this  $O(8)$  symmetry to transform the critical theory into a well-known form. The coupling term in the Majorana basis becomes  $g \vec{N} \cdot (\eta^T \tau^y \vec{\Sigma} \eta)$  with  $\vec{\Sigma} = (\sigma^z \rho^x, \rho^z, -\sigma^x \rho^x)$ , where the Pauli matrices  $\rho^{x,y,z}$  act in the Majorana space  $(\eta_1, \eta_2)$ . With an orthogonal transformation  $O = \frac{i}{\sqrt{2}} (\sigma^y \rho^z - \rho^y) \in O(8)$ , it can be transformed into  $g \vec{N} \cdot (\eta'^T \tau^y \vec{\Sigma}' \eta')$  with  $\eta' = O\eta$  and  $\vec{\Sigma}' = (\sigma^x, -\sigma^y \rho^y, \sigma^z)$ , which if written in terms of complex fermions, is nothing but the standard Gross-Neveu-Heisenberg coupling  $g \vec{N} \cdot (\Psi'^\dagger \tau^y \vec{\sigma} \Psi')$  where  $\Psi' = \eta'_1 + i\eta'_2$ . Therefore, the low energy theory is equivalent to the chiral Gross-Neveu-Heisenberg model, and the transition should also belong to the chiral Heisenberg universality class with two four-component Dirac fermions [47–56]. The critical exponents we found, namely  $\nu \approx 0.99$  and  $\eta_m \approx 0.55$ , are consistent with these previous works, although it's worth noting that the value of  $\eta_m$  reported in previous numerical works differ from each other considerably, and lies in a window ranging from 0.45 to 1.2, which likely signals strong finite-size corrections for this exponent.

*Discussion and conclusion*— Very broadly, our model is in the similar spirit as Refs.[57–61], where a desired ordered phase is obtained by coupling the corresponding fermionic bilinear to a fluctuating bosonic field, and then tuning the kinetic energy of the boson to obtain an order-disorder quantum critical point.

The competition between d-wave superconductivity and AFM is also explored in Monte Carlo studies of various multiband models [62–65]. In contrast to our model, where we obtain nodal superconductivity with repulsive onsite Hubbard- $U$ , in the models considered in Refs.[62–65], the pairing order-parameter is in fact onsite, and the superconductivity is generically not nodal. This is related to the fact that the repulsive onsite Hubbard- $U$  would lead to sign problem in these models. The d-wave-like form factor in these models resulted from a pairing of the form  $c_{i\uparrow x}^\dagger c_{i\downarrow x}^\dagger - c_{i\uparrow y}^\dagger c_{i\downarrow y}^\dagger$ , where  $i$  denotes a lattice site, and  $x, y$  denote two different bands, which have stronger hopping along the  $x$  and  $y$  directions respectively. We also note an interesting proposal for a model of competing AFM and nodal dSC phases, Ref.[66]. However, to our knowledge, this model cannot be analytically argued to host a dSC phase and furthermore, the value of the d-wave order-parameter obtained on the largest system size was rather small, making it unclear whether d-wave correlations persist in the thermodynamic limit.

Our study motivates several new directions. Our model allows for adding orbital and Zeeman magnetic fields of arbitrary strength *without* introducing sign-problem. It will be very interesting to study the destruction of dSC as either of these fields are ramped up. Another interesting question is to explore the possibility of destroying the dSC phase by proliferating *double* vortices,

while keeping a single vortex gapped. This will lead to a fractionalized phase with topological order where nodal spinons are coupled to a  $Z_2$  gauge field. In Ref.[34], such a phase was proposed as a candidate for the pseudogap phase in cuprates. One way to obtain such a phase is to supplement the Hamiltonian with additional terms that penalize single vortices, while allowing double vortices to condense [67, 68]. These additional terms do not cause sign-problem. Finally, it will be worthwhile to pursue an analogous model which does not contain the Cooper-pair field  $\theta$  explicitly, and where the microscopic degrees of freedom are purely electronic.

In summary, we constructed a sign-problem-free repulsive Hubbard model which hosts competing AFM and nodal d-wave phases. We found three different phases by tuning a single parameter  $K/J$  that controls the fluctuations of the bosonic fields: a nodal dSC phase at small  $K/J$ , an AFM phase at large  $K/J$ , and an intermediate phase with coexisting gapped d-wave and AFM orders. The phase transition between the coexistence phase and the AFM phase is a conventional 3D XY transition, while that between the coexistence phase and the nodal d-wave also appears to be continuous, and belongs to the 2+1-D Gross-Neveu-Heisenberg universality class. We studied various universal quantities associated with these transitions.

*Note added:* During the completion of this manuscript, we became aware of a recent preprint [arXiv:2009.04685](https://arxiv.org/abs/2009.04685) [69], which studies a *mean-field* Hamiltonian of nodal dSC with repulsive Hubbard- $U$ , i.e., a model where the charge  $U(1)$  symmetry is *explicitly* broken (and thus, there is no analog of the fluctuating field  $\theta$ ). Although this model doesn't support a phase where the superconductor results from spontaneous symmetry breaking, or an AFM phase which preserves charge  $U(1)$ , it can still be thought of as an effective description of the transition between the nodal dSC and the coexisting dSC<sub>g</sub>+AFM phase in our model. This is because the charge- $U(1)$  doesn't play an important role across this transition.

We thank Fakhre Assaad and John McGreevy for useful discussions. TG acknowledges support by the National Science Foundation under Grant No. DMR-1752417, and by an Alfred P. Sloan Research Fellowship.

---

[1] Michael R. Norman. The challenge of unconventional superconductivity. *Science*, 332(6026):196, 2011.  
 [2] E. Dagotto. *Rev. of Mod. Phys.*, 66:763, 1994.  
 [3] P.A. Lee, N. Nagaosa, and X.G. Wen. Doping a mott insulator: Physics of high-temperature superconductivity. *Rev. Mod. Phys.*, 78:17, 2006.  
 [4] F Steglich, CD Bredl, W Lieke, U Rauchschwalbe, and G Sparn. Heavy fermion superconductivity. *Physica B+C*, 126(1-3):82–91, 1984.

[5] G. R. Stewart. Heavy-fermion systems. *Rev. Mod. Phys.*, 56:755–787, Oct 1984.  
 [6] A. Amato. Heavy-fermion systems studied by  $\mu$ sr technique. *Rev. Mod. Phys.*, 69:1119–1180, Oct 1997.  
 [7] Christian Pfleiderer. Superconducting phases of  $f$ -electron compounds. *Rev. Mod. Phys.*, 81:1551–1624, Nov 2009.  
 [8] P. G. Pagliuso, C. Petrovic, R. Movshovich, D. Hall, M. F. Hundley, J. L. Sarrao, J. D. Thompson, and Z. Fisk. Coexistence of magnetism and superconductivity in  $\text{cerh}_{1-x}\text{ir}_x\text{in}_5$ . *Phys. Rev. B*, 64:100503, Aug 2001.  
 [9] M. Brian Maple, Ryan E. Baumbach, Nicholas P. Butch, James J. Hamlin, and Marc Janoschek. Non-fermi liquid regimes and superconductivity in the low temperature phase diagrams of strongly correlated  $d$ - and  $f$ -electron materials. *Journal of Low Temperature Physics*, 161(1), 2010.  
 [10] F. Steglich, J. Aarts, C. D. Bredl, W. Lieke, D. Meschede, W. Franz, and H. Schäfer. Superconductivity in the presence of strong pauli paramagnetism:  $\text{CeCu}_2\text{Si}_2$ . *Phys. Rev. Lett.*, 43(25):1892–1896, Dec 1979.  
 [11] Robert Joynt and Louis Taillefer. The superconducting phases of  $\text{Upt}_3$ . *Rev. Mod. Phys.*, 74:235–294, Mar 2002.  
 [12] G Knebel, M-A Méasson, B Salce, D Aoki, D Braithwaite, J P Brison, and J Flouquet. High-pressure phase diagrams of  $\text{CeRhIn}_5$  and  $\text{CeCoIn}_5$  studied by ac calorimetry. *Journal of Physics: Condensed Matter*, 16(49):8905–8922, nov 2004.  
 [13] Tuson Park, F. Ronning, H. Q. Yuan, M. B. Salamon, R. Movshovich, J. L. Sarrao, and J. D. Thompson. Hidden magnetism and quantum criticality in the heavy fermion superconductor  $\text{cerhin}_5$ . *Nature*, 440(7080):65–68, 2006.  
 [14] H. Q. Yuan, F. M. Grosche, M. Deppe, C. Geibel, G. Sparn, and F. Steglich. Observation of two distinct superconducting phases in  $\text{CeCu}_2\text{Si}_2$ . *Science*, 302(5653):2104–2107, 2003.  
 [15] T. Mito, S. Kawasaki, Y. Kawasaki, G. q. Zheng, Y. Kitaoka, D. Aoki, Y. Haga, and Y. Ōnuki. Coexistence of antiferromagnetism and superconductivity near the quantum criticality of the heavy-fermion compound  $\text{cerhins}_5$ . *Phys. Rev. Lett.*, 90:077004, Feb 2003.  
 [16] G. Aeppli, A. Goldman, G. Shirane, E. Bucher, and M.-Ch. Lux-Steiner. Development of antiferromagnetic correlations in the heavy-fermion system  $\text{Upt}_3$ . *Phys. Rev. Lett.*, 58:808–811, Feb 1987.  
 [17] F. Kagawa, K. Miyagawa, and K. Kanoda. Unconventional critical behaviour in a quasi-two-dimensional organic conductor. *Nature*, 436(7050):534–537, 07 2005.  
 [18] Y. Kurosaki, Y. Shimizu, K. Miyagawa, K. Kanoda, and G. Saito. Mott transition from a spin liquid to a fermi liquid in the spin-frustrated organic conductor  $\kappa-(\text{ET})_2\text{Cu}_2(\text{CN})_3$ . *Phys. Rev. Lett.*, 95:177001, Oct 2005.  
 [19] S. Lefebvre, P. Wzietek, S. Brown, C. Bourbonnais, D. Jérôme, C. Mézière, M. Fourmigué, and P. Batail. *Phys. Rev. Lett.*, 85:5420, 2000.  
 [20] T. Arai, K. Ichimura, K. Nomura, S. Takasaki, J. Yamada, S. Nakatsuji, and H. Anzai. Tunneling spectroscopy on the organic superconductor  $\kappa-(\text{BEDT}-\text{TTF})_2\text{Cu}(\text{NCS})_2$  using stm. *Phys. Rev. B*, 63:104518, Feb 2001.  
 [21] Stéphane Belin, Kamran Behnia, and André Deluzet. Heat conduction in  $\kappa-(\text{BEDT}-\text{TTF})_2\text{Cu}(\text{NCS})_2$ . *Phys.*

- Rev. Lett.*, 81:4728–4731, Nov 1998.
- [22] S. M. De Soto, C. P. Slichter, A. M. Kini, H. H. Wang, U. Geiser, and J. M. Williams.  $^{13}\text{C}$  nmr studies of the normal and superconducting states of the organic superconductor  $\kappa\text{-(et)}_2\text{cu}[\text{n}(\text{cn})_2]\text{br}$ . *Phys. Rev. B*, 52:10364–10368, Oct 1995.
- [23] H. Mayaffre, P. Wzietek, D. Jérôme, C. Lenoir, and P. Batail. Superconducting state of  $\kappa\text{-(ET)}_2\text{cu}[\text{n}(\text{CN})_2]\text{br}$  studied by  $^{13}\text{C}$  nmr: Evidence for vortex-core-induced nuclear relaxation and unconventional pairing. *Phys. Rev. Lett.*, 75:4122–4125, Nov 1995.
- [24] K. Kanoda, K. Miyagawa, A. Kawamoto, and Y. Nakazawa. Nmr relaxation rate in the superconducting state of the organic conductor  $\kappa\text{-(bedt-tf)}_2\text{cu}[\text{n}(\text{cn})_2]\text{br}$ . *Phys. Rev. B*, 54:76–79, Jul 1996.
- [25] D. JÉROME. The physics of organic superconductors. *Science*, 252(5012):1509–1514, 1991.
- [26] GR Stewart. Superconductivity in iron compounds. *Reviews of Modern Physics*, 83(4):1589, 2011.
- [27] Qimiao Si, Rong Yu, and Elihu Abrahams. High-temperature superconductivity in iron pnictides and chalcogenides. *Nature Reviews Materials*, 1(4):1–15, 2016.
- [28] Pengcheng Dai. Antiferromagnetic order and spin dynamics in iron-based superconductors. *Rev. Mod. Phys.*, 87:855–896, Aug 2015.
- [29] D. K. Pratt, W. Tian, A. Kreyssig, J. L. Zarestky, S. Nandi, N. Ni, S. L. Bud'ko, P. C. Canfield, A. I. Goldman, and R. J. McQueeney. Coexistence of competing antiferromagnetic and superconducting phases in the underdoped  $\text{Ba}(\text{fe}_{0.953}\text{co}_{0.047})_2\text{as}_2$  compound using x-ray and neutron scattering techniques. *Phys. Rev. Lett.*, 103:087001, Aug 2009.
- [30] S. Nandi, M. G. Kim, A. Kreyssig, R. M. Fernandes, D. K. Pratt, A. Thaler, N. Ni, S. L. Bud'ko, P. C. Canfield, J. Schmalian, R. J. McQueeney, and A. I. Goldman. Anomalous suppression of the orthorhombic lattice distortion in superconducting  $\text{Ba}(\text{fe}_{1-x}\text{co}_x)_2\text{as}_2$  single crystals. *Phys. Rev. Lett.*, 104:057006, Feb 2010.
- [31] Dieter Vollhardt and Peter Wolfe. *The superfluid phases of helium 3*. Courier Corporation, 2013.
- [32] Leon Balents, Cory R Dean, Dmitri K Efetov, and Andrea F Young. Superconductivity and strong correlations in moiré flat bands. *Nature Physics*, pages 1–9, 2020.
- [33] P. W. Anderson. The resonating valence bond state in  $\text{la}_2\text{cuo}_4$  and superconductivity. *Science*, 235(4793):1196–1198, 1987.
- [34] Leon Balents, Matthew PA Fisher, and Chetan Nayak. Nodal liquid theory of the pseudo-gap phase of high- $t$   $c$  superconductors. *International Journal of Modern Physics B*, 12(10):1033–1068, 1998.
- [35] Congjun Wu and Shou-Cheng Zhang. Sufficient condition for absence of the sign problem in the fermionic quantum monte carlo algorithm. *Phys. Rev. B*, 71:155115, Apr 2005.
- [36] Masaki Oshikawa. Commensurability, excitation gap, and topology in quantum many-particle systems on a periodic lattice. *Phys. Rev. Lett.*, 84(7):1535–1538, Feb 2000.
- [37] M. B. Hastings. Lieb-schultz-mattis in higher dimensions. *Phys. Rev. B*, 69(10):104431, Mar 2004.
- [38] A. I. Lichtenstein and M. I. Katsnelson. Antiferromagnetism and  $d$ -wave superconductivity in cuprates: A cluster dynamical mean-field theory. *Phys. Rev. B*, 62:R9283–R9286, Oct 2000.
- [39] M Jarrell, Th Maier, M. H Hettler, and A. N Tahvildarzadeh. Phase diagram of the hubbard model: Beyond the dynamical mean field. *Europhysics Letters (EPL)*, 56(4):563–569, nov 2001.
- [40] David Sénéchal, P.-L. Lavertu, M.-A. Marois, and A.-M. S. Tremblay. Competition between antiferromagnetism and superconductivity in high- $T_c$  cuprates. *Phys. Rev. Lett.*, 94:156404, Apr 2005.
- [41] M. Capone and G. Kotliar. Competition between  $d$ -wave superconductivity and antiferromagnetism in the two-dimensional hubbard model. *Phys. Rev. B*, 74:054513, Aug 2006.
- [42] Andriy H. Nevidomskyy, Christian Scheiber, David Sénéchal, and A.-M. S. Tremblay. Magnetism and  $d$ -wave superconductivity on the half-filled square lattice with frustration. *Phys. Rev. B*, 77:064427, Feb 2008.
- [43] S. S. Kancharla, B. Kyung, D. Sénéchal, M. Civelli, M. Capone, G. Kotliar, and A.-M. S. Tremblay. Anomalous superconductivity and its competition with antiferromagnetism in doped mott insulators. *Phys. Rev. B*, 77:184516, May 2008.
- [44] *See Supplemental Material(SM) for more details. The SM also contains additional Refs. [70–72].*
- [45] R. Blankenbecler, D. J. Scalapino, and R. L. Sugar. Monte carlo calculations of coupled boson-fermion systems. i. *Phys. Rev. D*, 24:2278–2286, Oct 1981.
- [46] F.F. Assaad and H.G. Evertz. World-line and determinantal quantum monte carlo methods for spins, phonons and electrons. In H. Fehske, R. Schneider, and A. Weiße, editors, *Computational Many-Particle Physics*, volume 739 of *Lecture Notes in Physics*, pages 277–356. Springer Berlin Heidelberg, 2008.
- [47] B. Rosenstein, Hoi-Lai Yu, and A. Kovner. Critical exponents of new universality classes. *Physics Letters B*, 314(3):381 – 386, 1993.
- [48] Igor F. Herbut. Interactions and phase transitions on graphene's honeycomb lattice. *Phys. Rev. Lett.*, 97:146401, October 2006.
- [49] Igor F. Herbut, Vladimir Juričić, and Bitan Roy. Theory of interacting electrons on the honeycomb lattice. *Phys. Rev. B*, 79:085116, Feb 2009.
- [50] Fakher F. Assaad and Igor F. Herbut. Pinning the order: The nature of quantum criticality in the hubbard model on honeycomb lattice. *Phys. Rev. X*, 3:031010, Aug 2013.
- [51] Francesco Parisen Toldin, Martin Hohenadler, Fakher F. Assaad, and Igor F. Herbut. Fermionic quantum criticality in honeycomb and  $\pi$ -flux hubbard models: Finite-size scaling of renormalization-group-invariant observables from quantum monte carlo. *Phys. Rev. B*, 91:165108, Apr 2015.
- [52] Yuichi Otsuka, Seiji Yunoki, and Sandro Sorella. Universal quantum criticality in the metal-insulator transition of two-dimensional interacting dirac electrons. *Phys. Rev. X*, 6:011029, Mar 2016.
- [53] Nikolai Zerf, Luminita N. Mihaila, Peter Marquard, Igor F. Herbut, and Michael M. Scherer. Four-loop critical exponents for the gross-neveu-yukawa models. *Phys. Rev. D*, 96:096010, Nov 2017.
- [54] J. A. Gracey. Large  $n$  critical exponents for the chiral heisenberg gross-neveu universality class. *Phys. Rev. D*, 97:105009, May 2018.
- [55] Pavel Buividovich, Dominik Smith, Maksim Ulybyshev,

- and Lorenz von Smekal. Hybrid monte carlo study of competing order in the extended fermionic hubbard model on the hexagonal lattice. *Phys. Rev. B*, 98:235129, Dec 2018.
- [56] Thomas C. Lang and Andreas M. Läuchli. Quantum monte carlo simulation of the chiral heisenberg gross-neveu-yukawa phase transition with a single dirac cone. *Phys. Rev. Lett.*, 123:137602, Sep 2019.
- [57] Erez Berg, Max A. Metlitski, and Subir Sachdev. Sign-problem-free quantum monte carlo of the onset of antiferromagnetism in metals. *Science*, 338(6114):1606–1609, 2012.
- [58] Y. Schattner, S. Lederer, S. A. Kivelson, and E. Berg. Ising nematic quantum critical point in a metal: a Monte Carlo study. *ArXiv e-prints*, November 2015.
- [59] Erez Berg, Samuel Lederer, Yoni Schattner, and Simon Trebst. Monte carlo studies of quantum critical metals. *Annual Review of Condensed Matter Physics*, 10(1):63–84, 2019.
- [60] Xiao Yan Xu, Zi Hong Liu, Gaopei Pan, Yang Qi, Kai Sun, and Zi Yang Meng. Revealing fermionic quantum criticality from new monte carlo techniques. *Journal of Physics: Condensed Matter*, 31(46):463001, aug 2019.
- [61] Zi-Xiang Li and Hong Yao. Sign-problem-free fermionic quantum monte carlo: Developments and applications. *Annual Review of Condensed Matter Physics*, 10(1):337–356, 2019.
- [62] Yoni Schattner, Max H. Gerlach, Simon Trebst, and Erez Berg. Competing orders in a nearly antiferromagnetic metal. *Phys. Rev. Lett.*, 117:097002, Aug 2016.
- [63] Philipp T Dumitrescu, Maksym Serbyn, Richard T Scalettar, and Ashvin Vishwanath. Superconductivity and nematic fluctuations in a model of doped fese monolayers: Determinant quantum monte carlo study. *Physical Review B*, 94(15):155127, 2016.
- [64] Zi-Xiang Li, Fa Wang, Hong Yao, and Dung-Hai Lee. Nature of the effective interaction in electron-doped cuprate superconductors: A sign-problem-free quantum monte carlo study. *Physical Review B*, 95(21):214505, 2017.
- [65] Samuel Lederer, Yoni Schattner, Erez Berg, and Steven A Kivelson. Superconductivity and non-fermi liquid behavior near a nematic quantum critical point. *Proceedings of the National Academy of Sciences*, 114(19):4905–4910, 2017.
- [66] Fakher F Assaad, Masatoshi Imada, and Douglas J Scalapino. Quantum transition between an antiferromagnetic mott insulator and d x 2- y 2 superconductor in two dimensions. *Physical review letters*, 77(22):4592, 1996.
- [67] T. Senthil and Matthew P. A. Fisher.  $Z_2$  gauge theory of electron fractionalization in strongly correlated systems. *Phys. Rev. B*, 62:7850–7881, Sep 2000.
- [68] Subir Sachdev. Topological order, emergent gauge fields, and fermi surface reconstruction. *Reports on Progress in Physics*, 82(1):014001, nov 2018.
- [69] Yuichi Otsuka, Kazuhiro Seki, Sandro Sorella, and Seiji Yunoki. Dirac electrons in the square lattice hubbard model with a  $d$ -wave pairing field: chiral heisenberg universality class revisited. *arXiv:2009.04685 [cond-mat.str-el]*, 2020.
- [70] JMJ Van Leeuwen, MSL du Croo de Jongh, and PJH Denteneer. Spin stiffness in the hubbard model. *Journal of Physics A: Mathematical and General*, 29(1):41, 1996.
- [71] Anders W. Sandvik. Stochastic method for analytic continuation of quantum monte carlo data. *Phys. Rev. B*, 57:10287–10290, May 1998.
- [72] F. F. Assaad. Phase diagram of the half-filled two-dimensional  $SU(n)$  hubbard-heisenberg model: A quantum monte carlo study. *Phys. Rev. B*, 71:075103, Feb 2005.

**Supplemental Material for "Competing nodal d-wave superconductivity and antiferromagnetism: a Quantum Monte Carlo study"**

**I. MEAN-FIELD THEORY**

As discussed in the main text, the Hamiltonian of our model is:  $H = H_t + H_U + H_V + H_{XY}$  with

$$H_t = -t \sum_{\langle ij \rangle, \sigma} (c_{i,\sigma}^\dagger c_{j,\sigma} + \text{h.c.}) \quad (\text{S1})$$

$$H_U = -\frac{U}{2} \sum_i (\rho_{i,\uparrow} + \rho_{i,\downarrow} - 1)^2 \quad (\text{S2})$$

$$H_V = V \sum_{\langle ij \rangle} (\tau_{i,j} e^{i\theta_{i,j}} (c_{i,\uparrow}^\dagger c_{j,\downarrow}^\dagger - c_{j,\uparrow}^\dagger c_{i,\downarrow}^\dagger) + \text{h.c.}) \quad (\text{S3})$$

$$H_{XY} = K \sum_{\langle ij \rangle} n_{ij}^2 - J \sum_{\langle ij,kl \rangle} \cos(\theta_{ij} - \theta_{kl}), \quad (\text{S4})$$

Let's define  $\hat{\alpha}_{ij} \equiv -e^{i\theta_{ij}}$ ,  $\hat{\Delta}_{ij} \equiv \tau_{i,j} (c_{i,\uparrow}^\dagger c_{j,\downarrow}^\dagger - c_{i,\downarrow}^\dagger c_{j,\uparrow}^\dagger)$ . We consider mean-field order parameters  $\alpha = \langle \hat{\alpha}_{ij} \rangle$ ,  $\Delta = \langle \hat{\Delta}_{ij} \rangle$  and  $m = (-)^i \langle (\rho_{i,\uparrow} - \rho_{i,\downarrow}) \rangle$ , leading to two coupled mean-field Hamiltonians. For fermions  $c$  we have,

$$\begin{aligned} H_f^{\text{MF}} = & -t \sum_{\langle ij \rangle, \sigma} (c_{i,\sigma}^\dagger c_{j,\sigma} + \text{h.c.}) - Um \sum_i (-)^i (\rho_{i,\uparrow} - \rho_{i,\downarrow}) \\ & - V\alpha \sum_{\langle ij \rangle} (\hat{\Delta}_{ij} + \text{h.c.}) \end{aligned} \quad (\text{S5})$$

For rotors  $\theta$  we have,

$$\begin{aligned} H_\theta^{\text{MF}} = & K \sum_{\langle ij \rangle} n_{ij}^2 - J \sum_{\langle ij,kl \rangle} \cos(\theta_{ij} - \theta_{kl}) \\ & - V\Delta \sum_{\langle ij \rangle} (\hat{\alpha}_{ij} + \text{h.c.}) \end{aligned} \quad (\text{S6})$$

We solve the two coupled mean-field Hamiltonians self-consistently.

$H_\theta^{\text{MF}}$  part can be solved with numerical exact diagonalization (ED). We consider  $\theta$  fields living on only four bonds of a square plaquette, and solve the four-bond-problem with ED. Choosing an eigenbasis of  $n_\delta$ ,  $n_\delta |l\rangle = l|l\rangle$ , we truncate  $|l| \leq l_c$ . (The results converge rather fast with  $l_c$  and  $l_c = 4$  turned out to be sufficient). We first solve the following eigenvalue problem

$$H_\theta^{\text{MF}} |\psi_i(\theta)\rangle = E_i |\psi_i(\theta)\rangle, \quad (\text{S7})$$

and obtain a self-consistent equation for  $\alpha$ :

$$\alpha = \frac{\sum_i \langle \psi_i(\theta) | \hat{\alpha} | \psi_i(\theta) \rangle e^{-\beta E_i}}{\sum_i e^{-\beta E_i}}. \quad (\text{S8})$$

The fermion mean-field Hamiltonian  $H_f^{\text{MF}}$  is quadratic, and can be diagonalized in a straightforward manner. This leads to self-consistent equations for  $m$  and  $\Delta$ :

$$m = \frac{U}{N} \sum_k \frac{m}{E(\vec{k})} \left( \frac{1}{e^{-\beta E(\vec{k})} + 1} - \frac{1}{e^{\beta E(\vec{k})} + 1} \right) \quad (\text{S9})$$

$$\Delta = \frac{2V\alpha}{N} \sum_k \frac{(\cos k_x - \cos k_y)^2}{E(\vec{k})} \left( \frac{1}{e^{-\beta E(\vec{k})} + 1} - \frac{1}{e^{\beta E(\vec{k})} + 1} \right) \quad (\text{S10})$$



where  $E(\vec{k}) = \sqrt{\epsilon^2(\vec{k}) + \Delta^2(\vec{k}) + m^2 U^2}$  with kinetic energy  $\epsilon(\vec{k}) = -2t(\cos k_x + \cos k_y)$ , and the gap equation  $\Delta(\vec{k}) = -2V\alpha(\cos k_x - \cos k_y)$ . We solve the fermion and the rotor mean-field equations self-consistently to obtain the eventual mean-field solution. In the calculation, we set  $t = 1$ ,  $J = 1$ ,  $V/t = 0.5$ , and explore the  $U/t - K/J$  ground state phase diagram as shown in Fig. 1(a) of the main text.

## II. DETERMINANTAL QUANTUM MONTE CARLO SIMULATION

In this section, we present the details of the Determinantal Quantum Monte Carlo (DQMC) algorithm. Let's consider a new basis,  $(\tilde{c}_{i,\uparrow}^\dagger, \tilde{c}_{i,\downarrow}^\dagger) \equiv (c_{i,\uparrow}^\dagger, \epsilon_i c_{i,\downarrow})$ , then the Hamiltonian becomes  $H = H_t + H_V + H_U + H_{XY}$ , with

$$H_t = -t \sum_{\langle ij \rangle, \sigma} (\tilde{c}_{i,\sigma}^\dagger \tilde{c}_{j,\sigma} + \text{h.c.}) \quad (\text{S11})$$

$$H_V = -V \sum_{\langle ij \rangle} (\tau_{i,j} e^{i\theta_{i,j}} \epsilon_i (\tilde{c}_{i,\uparrow}^\dagger \tilde{c}_{j,\downarrow} - \tilde{c}_{j,\uparrow}^\dagger \tilde{c}_{i,\downarrow}) + \text{h.c.}) \quad (\text{S12})$$

$$H_U = -\frac{U}{2} \sum_i (\tilde{\rho}_{i,\uparrow} + \tilde{\rho}_{i,\downarrow} - 1)^2 \quad (\text{S13})$$

$$H_{XY} = K \sum_{\langle ij \rangle} n_{ij}^2 - J \sum_{\langle ij, kl \rangle} \cos(\theta_{ij} - \theta_{kl}), \quad (\text{S14})$$

where  $\tilde{\rho}_{i,\sigma} = \tilde{c}_{i,\sigma}^\dagger \tilde{c}_{i,\sigma}$ . We consider a square lattice with system size  $N = L \times L$ . To simulate this model by DQMC, we start with the partition function  $\mathcal{Z} = \text{Tr}(e^{-\beta H})$ , and perform the Trotter decomposition to divide the imaginary time evolution into  $L_\tau$  slices  $\beta = L_\tau \Delta_\tau$ . Then we do further Trotter decomposition to separate the hopping part, the coupling part and the Hubbard interaction part. To deal with the Hubbard interaction part, we introduce the following Hubbard-Stratonovich (HS) transformation [72]:

$$e^{\Delta_\tau \frac{U}{2} (\tilde{\rho}_{i,\uparrow} + \tilde{\rho}_{i,\downarrow} - 1)^2} = \frac{1}{4} \sum_{\{s_i\}} \gamma(s_i) e^{\alpha \eta(s_i) (\tilde{\rho}_{i,\uparrow} + \tilde{\rho}_{i,\downarrow} - 1)} \quad (\text{S15})$$

with  $\alpha = \sqrt{\Delta_\tau \frac{U}{2}}$ ,  $\gamma(\pm 1) = 1 + \sqrt{6}/3$ ,  $\gamma(\pm 2) = 1 - \sqrt{6}/3$ ,  $\eta(\pm 1) = \pm \sqrt{2(3 - \sqrt{6})}$ ,  $\eta(\pm 2) = \pm \sqrt{2(3 + \sqrt{6})}$ . Then we have the following fermion bilinear at time slice  $\tau$ ,

$$\begin{aligned} H_\tau &= \sum_i \alpha \eta(s_{i,\tau}) (\tilde{\rho}_{i,\uparrow} + \tilde{\rho}_{i,\downarrow} - 1) \\ &\quad + \Delta_\tau V \sum_{\langle ij \rangle} (\tau_{i,j} \epsilon_i e^{i\theta_{ij}(\tau)} (\tilde{c}_{i,\uparrow}^\dagger \tilde{c}_{j,\downarrow} - \tilde{c}_{i,\downarrow}^\dagger \tilde{c}_{j,\uparrow}) + \text{h.c.}) \\ &\quad + \Delta_\tau t \sum_{\langle ij \rangle} (\tilde{c}_{i,\alpha}^\dagger \tilde{c}_{j,\alpha} + \text{h.c.}) \\ &\equiv \tilde{\mathbf{c}}^\dagger \mathbf{K}_U \tilde{\mathbf{c}} + \tilde{\mathbf{c}}^\dagger \mathbf{V}_\Delta \tilde{\mathbf{c}} + \tilde{\mathbf{c}}^\dagger \mathbf{K}_t \tilde{\mathbf{c}} \end{aligned} \quad (\text{S16})$$

where  $\tilde{\mathbf{c}} = (\tilde{c}_{1,\uparrow}, \tilde{c}_{1,\downarrow}, \dots, \tilde{c}_{N,\uparrow}, \tilde{c}_{N,\downarrow})^T$ , and  $\mathbf{K}_U$ ,  $\mathbf{V}_\Delta$  and  $\mathbf{K}_t$  are the corresponding matrices of the three kinds of fermion bilinears. Consider the antiunitary time reversal transformation:  $\tilde{c}_{i,\uparrow} \rightarrow \tilde{c}_{i,\downarrow}$ ,  $\tilde{c}_{i,\downarrow} \rightarrow -\tilde{c}_{i,\uparrow}$ ,  $\sqrt{-1} \rightarrow -\sqrt{-1}$ . It is easy to check that  $\tilde{\mathbf{c}}^\dagger \mathbf{K}_U \tilde{\mathbf{c}}$ ,  $\tilde{\mathbf{c}}^\dagger \mathbf{V}_\Delta \tilde{\mathbf{c}}$  and  $\tilde{\mathbf{c}}^\dagger \mathbf{K}_t \tilde{\mathbf{c}}$  are all invariant under this transformation. This proves that tracing out fermions in the partition function does not lead to a sign problem [35]. Next, we will show that  $H_{XY}$  contribution to the partition function is also sign-problem-free, thereby proving that the full Hamiltonian is sign-problem-free.

Now let us consider  $H_{XY}$ . It is convenient to work in a basis where  $\theta_{ij}$  is diagonal,  $\theta|\theta\rangle = \theta|\theta\rangle$ . As  $[n_{ij}, e^{\pm i\theta_{ij}}] = \pm e^{\pm i\theta_{ij}}$ ,  $n_{ij}$  behaves like  $n_{ij} = -i \frac{\partial}{\partial \theta_{i,j}}$ . Denoting eigenbasis of  $n_{ij}$  as  $|n_{ij}\rangle$ , we have  $\langle \theta | n \rangle = e^{i\theta n}$ . This implies

$$\langle \theta' | e^{-\Delta_\tau K n^2} | \theta \rangle \sim e^{\frac{1}{2\Delta_\tau K} \cos(\theta - \theta')} \quad (\text{S17})$$

We can now evaluate the partition function

$$\begin{aligned}
\mathcal{Z} &= \text{Tr} \left( e^{-\beta H} \right) \\
&= \text{Tr}_F \sum_{\{\theta\}} \langle \theta_{\tau=1} | e^{-\Delta\tau H} | \theta_{\tau=L_\tau} \rangle \langle \theta_{\tau=L_\tau} | e^{-\Delta\tau H} | \theta_{\tau=L_\tau-1} \rangle \cdots \langle \theta_{\tau=2} | e^{-\Delta\tau H} | \theta_{\tau=1} \rangle \\
&= \sum_{\{\theta, s\}} e^{\frac{1}{2\Delta\tau K} \sum_{\langle ij, \tau \rangle} \cos(\theta_{ij, \tau+1} - \theta_{ij, \tau}) + \Delta\tau J \sum_{\langle ij, kl, \tau \rangle} \cos(\theta_{ij, \tau} - \theta_{kl, \tau})} \left( \prod_{i, \tau} \gamma(s_{i, \tau}) e^{-\alpha\eta(s_{i, \tau})} \right) \det \left( \mathbf{1} + \prod_{\tau} \mathbf{B}_\tau \right) \quad (\text{S18})
\end{aligned}$$

with  $\mathbf{B}_\tau = e^{\mathbf{K}_U} e^{\mathbf{V}_\Delta} e^{\mathbf{K}_t}$ . The first part of the last equation corresponds to an anisotropic XY model. We denote the configurations  $\{\theta, s\}$  as  $\mathcal{C}$ , and write their weight as  $\omega_{\mathcal{C}} = \omega_{\mathcal{C}}^I \omega_{\mathcal{C}}^{II}$ , with

$$\omega_{\mathcal{C}}^I = e^{\frac{1}{2\Delta\tau K} \sum_{\langle ij, \tau \rangle} \cos(\theta_{ij, \tau+1} - \theta_{ij, \tau}) + \Delta\tau J \sum_{\langle ij, kl, \tau \rangle} \cos(\theta_{ij, \tau} - \theta_{kl, \tau})} \left( \prod_{i, \tau} \gamma(s_{i, \tau}) e^{-\alpha\eta(s_{i, \tau})} \right) \quad (\text{S19})$$

$$\omega_{\mathcal{C}}^{II} = \det \left( \mathbf{1} + \prod_{\tau} \mathbf{B}_\tau \right) \quad (\text{S20})$$

It is obvious that  $\omega_{\mathcal{C}}^I$  is sign-problem-free, while  $\omega_{\mathcal{C}}^{II}$  was already shown to be sign-problem-free using antiunitary time reversal symmetry. Thus, as promised, the model we simulate is sign problem free.

*Monte Carlo updates:* We update the auxiliary fields locally in DQMC. There are two kinds of auxiliary fields to be updated. For  $s_{i, \tau}$ , as it appears only along the diagonal of  $\mathbf{K}_U$ , a local change can be made as:

$$e^{\mathbf{K}'_U} = (\mathbf{1} + \mathbf{\Delta}) e^{\mathbf{K}_U} \quad (\text{S21})$$

where  $\mathbf{\Delta}$  has only two nonzero elements  $\mathbf{\Delta}_{i\uparrow, i\uparrow}$  and  $\mathbf{\Delta}_{i\downarrow, i\downarrow}$ . Let's define  $\mathbf{B}(\tau', \tau) \equiv \mathbf{B}_{\tau'} \cdots \mathbf{B}_\tau$ , and note that the equal-time Green's function  $\mathbf{G}(\tau, \tau) = (\mathbf{1} + \mathbf{B}(\tau, 0)\mathbf{B}(\beta, \tau))^{-1}$ . With a local update, we have

$$\frac{\omega_{\mathcal{C}'}^{II}}{\omega_{\mathcal{C}}^{II}} = \det[\mathbf{1} + \mathbf{\Delta}(\mathbf{1} - \mathbf{G}(\tau, \tau))] \quad (\text{S22})$$

and the ratio  $\frac{\omega_{\mathcal{C}'}^I}{\omega_{\mathcal{C}}^I}$  is straightforward to evaluate. If the local update is accepted, we update the equal-time Green's function as

$$\mathbf{G}'(\tau, \tau) = \mathbf{G}(\tau, \tau)[\mathbf{1} + \mathbf{\Delta}(\mathbf{1} - \mathbf{G})] \quad (\text{S23})$$

Due to the sparse nature of  $\mathbf{\Delta}$ , the fast update algorithm using Sherman–Morrison–Woodbury formula applies. The update for the  $\theta$  fields are very similar, the only difference is that  $\mathbf{\Delta}$  is different.

*Measurements in Monte Carlo:* Given equal-time Green's functions, one can use Wick's theorem to measure various static quantities, such as the energy and correlation functions of spins, d-wave pairing order parameters, and so on. In addition to static calculations, we also calculate dynamic properties, using imaginary time-displaced Green's function, again using Wick's theorem. In particular, we measure the time-displaced single particle Green's functions and the time-displaced spin correlations. Further technical details about the updates and measurements in DQMC can be found in Refs. [45, 46].

### III. CHARGE STIFFNESS AT THE XY TRANSITION

As discussed in the main text, the transition from dSC<sub>g</sub>+AFM to AFM is a 3D XY transition, which predicts universal behavior of charge stiffness with the tuning parameter. In the following, we derive the formula to measure the charge stiffness following the method described in Ref. [70].

By definition, the stiffness measures the free-energy increment associated with twisting the direction of the order parameter. For the transition from dSC<sub>g</sub>+AFM to AFM, the order parameter can be defined as  $\langle e^{i\theta_{ij}} \rangle$ . We consider a twist  $\theta_{ij} \rightarrow \theta_{ij} - \vec{q} \cdot \vec{r}_{ij}$ , and the stiffness is calculated as the second derivative of the free-energy with respect to

this twist:

$$\bar{\rho}_s = \frac{1}{N} \left. \frac{\partial^2 F(\phi)}{\partial \vec{q} \partial \vec{q}} \right|_{\vec{q}=0} \quad (\text{S24})$$

More explicitly, we expand the relevant part of the Hamiltonian in powers of  $i\vec{q}$ , so that we have

$$H'_{XY} = H_{XY} + i\vec{q} \cdot \vec{H}_{XY,1} + \frac{1}{2} i\vec{q} \cdot \vec{H}_{XY,2} \cdot i\vec{q} \quad (\text{S25})$$

where  $\vec{H}_{XY,1} = iJ \sum_{\langle ij,kl \rangle} \vec{r}_{ij,kl} \sin(\theta_{ij} - \theta_{kl})$  can be thought of as a current operator and  $\vec{H}_{XY,2} = -J \sum_{\langle ij,kl \rangle} \vec{r}_{ij,kl} \vec{r}_{ij,kl} \cos(\theta_{ij} - \theta_{kl})$ . The free energy increment due to  $\vec{q}$  can be calculated using perturbation theory

$$\delta F = \frac{1}{2} i\vec{q} \cdot \left\{ \langle \vec{H}_{XY,2} \rangle - \int_0^\beta \langle \vec{H}_{XY,1}(\tau) \vec{H}_{XY,1}(0) \rangle \right\} \cdot i\vec{q} \quad (\text{S26})$$

Where we have used that  $\langle \vec{H}_{XY,1} \rangle = 0$ . Thus we obtain

$$\bar{\rho}_s = -\frac{1}{N} \left\{ \langle \vec{H}_{XY,2} \rangle - \int_0^\beta \langle \vec{H}_{XY,1}(\tau) \vec{H}_{XY,1}(0) \rangle \right\} \quad (\text{S27})$$

Due to the  $\pi/2$  rotation symmetry of the square lattice,  $\bar{\rho}_s = \rho_s \vec{I}$ , and we can consider the twist along either direction. Let us take  $x$ -direction as an example, and we obtain

$$\rho_s = -\frac{1}{N} \left\{ \langle H_{XY,2}^x \rangle - \int_0^\beta \langle H_{XY,1}^x(\tau) H_{XY,1}^x(0) \rangle \right\} \quad (\text{S28})$$

where  $H_{XY,1}^x = iJ \sum_{\langle ij,kl \rangle} x_{ij,kl} \sin(\theta_{ij} - \theta_{kl})$ ,  $H_{XY,2}^x = -J \sum_{\langle ij,kl \rangle} \frac{1}{4} \cos(\theta_{ij} - \theta_{kl})$ .

### A. Stiffness of the pure rotor model

To test above formula within our simulations, we first consider the pure rotor model described by the Hamiltonian  $H_{XY}$ . As is well-known, and we already showed above explicitly using Trotter decomposition, the (2+1)D pure rotor model can be mapped to 3D XY model so that it has a 3D XY transition. Therefore we expect the associated universal critical behavior of the stiffness with respect to the tuning parameter  $K/J$ . As shown in Fig. S1, our simulation of this pure rotor model indeed finds that the data for stiffness can be collapsed with the 3D XY exponents.

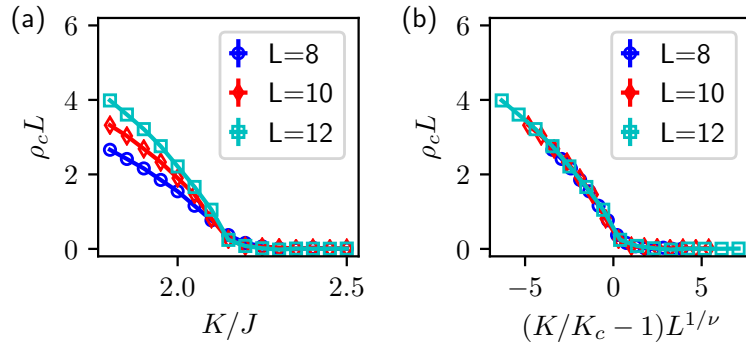


FIG. S1. Charge stiffness of the pure (2+1)D rotor model.  $K_c \approx 2.13$ ,  $\nu \approx 0.67$ .

## B. Stiffness of interacting model and finite temperature transition

The stiffness of our full, interacting model with  $\beta t = 2L$  is shown in Figs. 3(a) and (b), which is still well collapsed with 3D XY exponents, indicating that the transition is continuous and belongs to the 3D XY universality. The charge stiffness is also a good quantity to characterize finite temperature Berezinskii–Kosterlitz–Thouless (BKT) transition phase boundary. Based on the free energy argument of a single vortex, the BKT transition is determined by  $\rho_c = \frac{2T_c}{\pi}$ , see Figs. S2(a)-(g). The BKT phase boundary is plotted in Fig. S2(h).

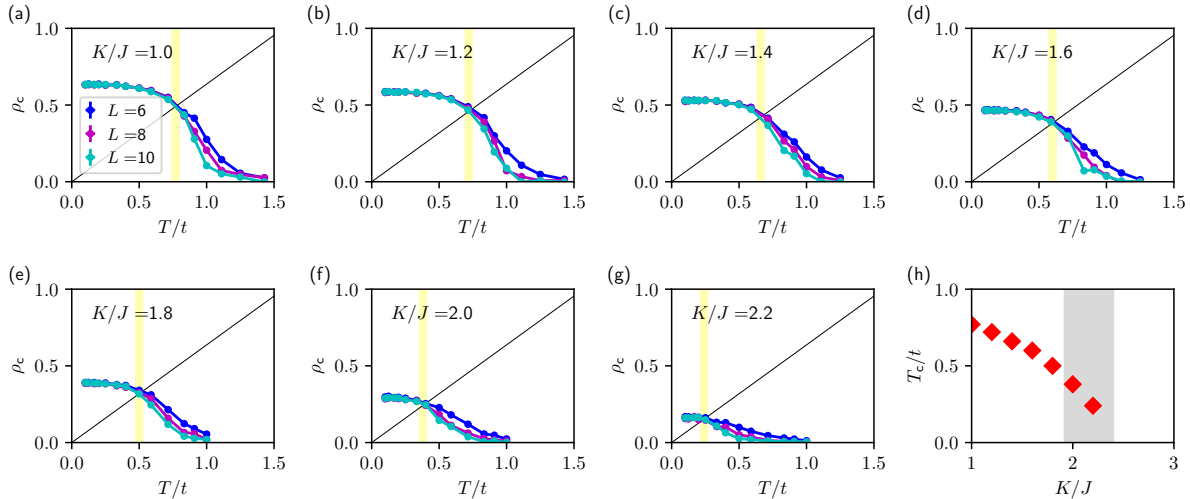


FIG. S2. Using charge stiffness to determine BKT phase transition boundary. (a)-(g) Charge stiffness for  $K/J = 1.0, 1.2, 1.4, 1.6, 1.8, 2.0, 2.2$ . (h) BKT phase transition boundary.

## IV. DETERMINING ZERO TEMPERATURE PHASE DIAGRAM

### A. dSC order parameters

The dSC order parameter  $\alpha$  defined as  $\alpha = \langle \hat{\alpha}_{ij} \rangle$  can be measured through the static correlation function

$$\alpha^2 = \frac{1}{4L^4} \sum_{\langle ij \rangle, \langle kl \rangle} \langle e^{i\theta_{ij}} e^{i\theta_{kl}} \rangle. \quad (\text{S29})$$

We perform a finite size scaling of  $\alpha^2$  to estimate its value in the thermodynamic limit, as shown in Fig. S3. We find that the dSC order parameter vanishes for  $K/J \geq 2.40(5)$ .

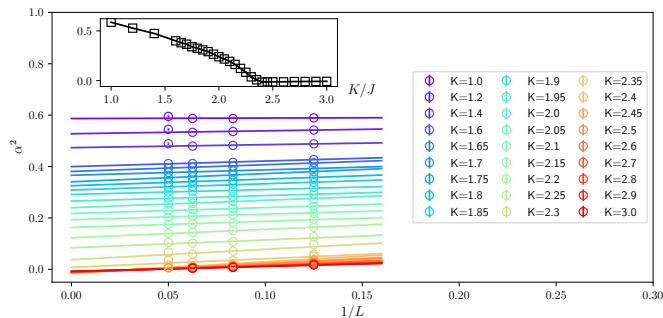


FIG. S3. Finite size scaling of  $\alpha^2$ .

### B. AFM order parameters

The AFM order parameter defined as  $\vec{m} = \langle (-)^i \vec{S}_i \rangle$  can be measured through static correlation function

$$m^2 = \frac{1}{L^4} \sum_{i,j} (-)^{i+j} \langle \vec{S}_i \cdot \vec{S}_j \rangle. \quad (\text{S30})$$

Again, we perform a finite size scaling of  $m^2$  to estimate its value in the thermodynamic limit, as shown in Fig. S4. The AFM order parameter vanishes for  $K/J \leq 1.92(5)$ .

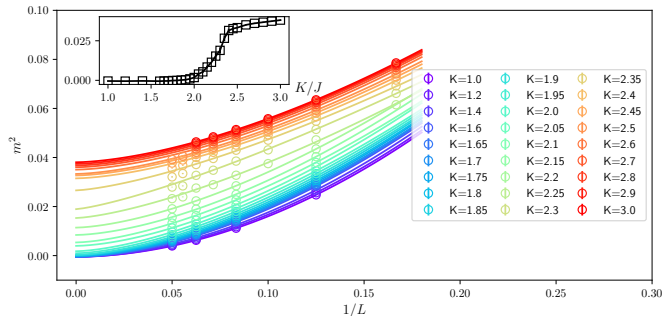


FIG. S4. Finite size scaling of  $m^2$ .

### C. Single-particle gap

The single-particle gap  $E_g(\vec{k})$  can be measured by extracting the slope of the decay of the time-displaced single particle Green's functions, based on the equation

$$\langle c(\vec{k}, \tau) c^\dagger(\vec{k}, 0) \rangle \sim e^{-E_g(\vec{k})\tau}, \quad (\text{S31})$$

where a sum over spin index is implicit. After we obtain the single-particle gap for each finite size  $L$ , we perform a  $1/L$  extrapolation to obtain its value in the thermodynamic limit. In Fig. S5 we show the single particle gap at the K point. The single-particle gap opens around  $K/J = 1.92(5)$  where the AFM order parameter starts to rise. Therefore, between  $K/J = 1.92(5)$  and  $K/J = 2.40(5)$ , we have a coexistence of gapped dSC and AFM, which is denoted as the dSC<sub>g</sub>+AFM phase in the main text.

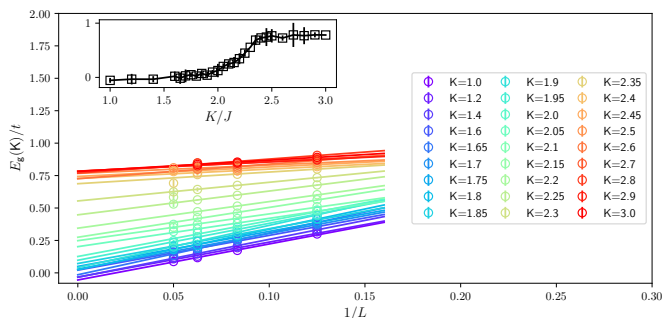


FIG. S5. Finite size scaling of the single-particle gap at the K point.

On the other hand, we still need to confirm that the dSC phase with  $K/J$  less than 1.92(5) is nodal, and that a full Fermi surface is absent. We explore the single-particle gap along different momentum paths, and confirm that only the four K points are gapless, as shown in Fig. 2(c). We also perform a more rigorous finite size scaling of the

single-particle gap at X point, the ‘anti-nodal’ point, to confirm that this point is indeed gapped in the nodal dSC phase, as shown in Fig. S6.

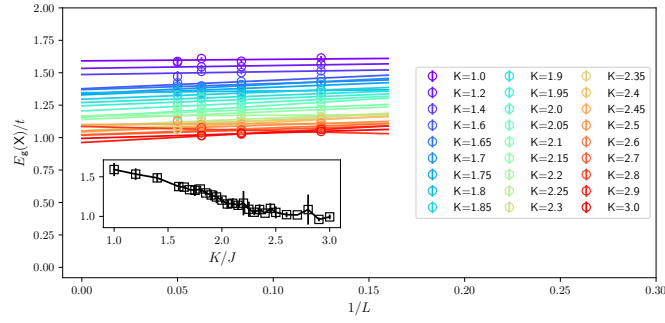


FIG. S6. Finite size scaling of single-particle gap at the X point.

Furthermore, based on the mean-field theory, the anti-nodal gap is predicted to be  $E(X) = \sqrt{16V^2\alpha^2 + m^2U^2}$ . As we already extracted the value of both  $\alpha^2$  and  $m^2$  using DQMC, we can compare the mean-field predicted anti-nodal gap with the estimation from time-displaced Green’s functions. As shown in Fig. S7, the mean-field estimate and the actual gap overall track each other rather well. The deviation is larger close to the XY transition, presumably because of larger fluctuations.

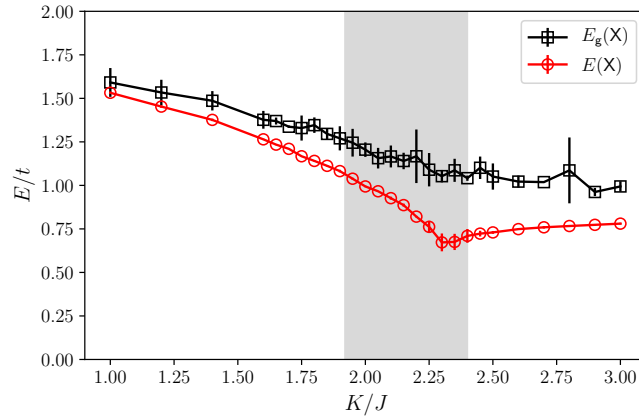


FIG. S7. Comparison of the the mean-field predicted anti-nodal gap with the estimation from time-displaced Green’s functions.

## V. SPIN GAP

Similar to the single-particle gap, the spin-gap  $E_s(\vec{k})$  can be measured by extracting the slope of the decay of the time-displaced spin correlation functions using

$$\langle \vec{S}(\vec{k}, \tau) \cdot \vec{S}(-\vec{k}, 0) \rangle \sim e^{-E_s(\vec{k})\tau}. \quad (\text{S32})$$

## VI. EXTRACTING FERMI VELOCITY, PAIRING VELOCITY AND SPIN-WAVE VELOCITY

Based on the estimation of the single-particle gap  $E_g(\vec{k})$  and the spin-gap  $E_s(\vec{k})$ , we can extract the Fermi velocity  $v_F$ , the pairing velocity  $v_\Delta$  and the spin-wave velocity  $v_s$ . Denote  $d\vec{k}_1$  as the smallest momentum along the K-M direction, and  $d\vec{k}_2$  the smallest momentum along the K-Y direction (see Fig.2(a) for the definition of various

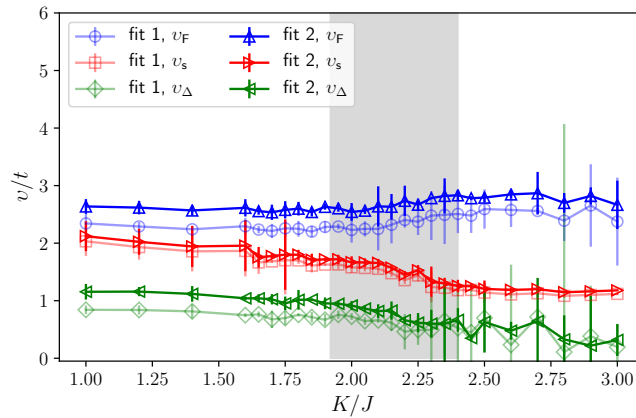


FIG. S8. The three velocities  $v_F, v_s, v_\Delta$  obtained using the two schemes discussed in the main text (Fig. 2(e)).

points in the Brillouin zone). Based on the low energy theory, we have  $E_g(\vec{q}') = \sqrt{v_F^2 q_x'^2 + v_\Delta^2 q_y'^2 + E_g^2(K)}$  and  $E_s(\vec{q}') = \sqrt{v_s^2 q'^2 + E_s^2(M)}$ . Therefore we can use following formulas to extract velocities:

$$v_F = \sqrt{\frac{E_g^2(K + \vec{d}\vec{k}_1) - E_g^2(K)}{|\vec{d}\vec{k}_1|^2}} \quad (\text{S33})$$

$$v_\Delta = \sqrt{\frac{E_g^2(K + \vec{d}\vec{k}_2) - E_g^2(K)}{|\vec{d}\vec{k}_2|^2}} \quad (\text{S34})$$

$$v_s = \sqrt{\frac{E_s^2(M + \vec{d}\vec{k}_1) - E_s^2(M)}{|\vec{d}\vec{k}_1|^2}} \quad (\text{S35})$$

with  $\vec{d}\vec{k}_1 = (\delta q, \delta q)$ ,  $\vec{d}\vec{k}_2 = (-\delta q, \delta q)$  and  $\delta q = \frac{2\pi}{L}$ . We considered two schemes to perform the finite size scaling. In scheme 1, we fix  $\delta q = \frac{2\pi}{L_{\max}}$ , and for system sizes less than  $L_{\max} = 20$ ,  $E_g(K + \vec{d}\vec{k}_1)$ ,  $E_g(K + \vec{d}\vec{k}_2)$  and  $E_s(\Gamma + \vec{d}\vec{k}_1)$  are obtained by interpolation. After we obtain the gap functions for each system size, we perform a  $1/L$  extrapolation of the gap, and finally use the above formulas to obtain the velocities. In scheme 2, we first calculate the velocities based on the above formulas for different system sizes  $L$  (that is  $\delta q = \frac{2\pi}{L}$  is not fixed), and then perform a  $1/L$  extrapolation of the velocities. The velocities we get from both schemes are shown in Fig. S8, which is a zoomed out version of Fig. 2(e). In principle, in the large  $L_{\max}$  limit, both schemes should yield same value for the velocities. However, in finite size calculations, as we can see that the scheme 1 comparatively yields smaller values. This may be understood as follows: the Dirac cones have a rather large curvature near the nodes as sketched in Fig. S9. Consider expanding the energy  $E$  to the second order in  $q'_x$  near the node,  $E = v_F q'_x + \frac{1}{2} c q_x'^2$  with curvature  $c < 0$  and we have assumed  $q'_x \geq 0$  for concreteness. At this order, for scheme 1 we find  $v_F^{\text{scheme 1}} = v_F + \frac{c\pi}{L_{\max}} < v_F$ . In contrast, for scheme 2 we find  $v_F^{\text{scheme 2}} = v_F + \frac{c\pi}{L}$  for each system size  $L$ , and it extrapolates to  $v_F$  when  $1/L$  is extrapolated to zero.

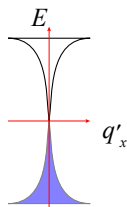


FIG. S9. The curvature of the Dirac dispersion can lead to finite size effects in extracting the velocities, as discussed in the accompanying text.

## VII. ANALYTICAL CONTINUATION TO GET SINGLE PARTICLE AND SPIN SPECTRUM

We use stochastic analytical continuation method [71] to extract the real frequency spectrum of both the single-particle and the spin. The analytic continuation is based on solving an inverse problem: given the imaginary time Green's functions  $G(\tau)$ , the task is to obtain the real frequency spectrum  $\rho(\omega)$ . These quantities are related by

$$G(\tau) = \int \frac{d\omega}{2\pi} \frac{\rho(\omega)e^{-\omega\tau}}{e^{-\beta\omega} \pm 1} \quad (\text{S36})$$

where  $\pm$  is for the fermionic and the bosonic case, respectively. In Fig. 2(a), we show the single-particle spectrum integrated over a small energy window near the Fermi level to find the location of the Dirac nodes inside the nodal dSC phase.